Zintl-phase Eu₂ZnSb₂: A promising thermoelectric material with ultralow thermal conductivity

Chen Chen[a,b], Wenhua Xue[c], Shan Li[a,b], Zongwei Zhang[a,b], Xiaofang Li[a,b], Xinyu Wang[a,b], Yijie Liu[d], Jiehe Sui[e], Xingjun Liu[a,b,e], Feng Cao[d], Zhifeng Ren[f], Ching-Wu Chu[f,1], Yumei Wang[c,1], and Qian Zhang[a,b,1]

[a]Department of Materials Science and Engineering, Harbin Institute of Technology, 518055 Shenzhen, People's Republic of China; [b]Institute of Materials Genome & Big Data, Harbin Institute of Technology, 518055 Shenzhen, People's Republic of China; [c]Beijing National Laboratory for Condensed Matter Physics, Institute of Physics, Chinese Academy of Science, 100190 Beijing, People's Republic of China; [d]School of Science, Harbin Institute of Technology, 518055 Shenzhen, People's Republic of China; [e]State Key Laboratory of Advanced Welding and Joining, Harbin Institute of Technology, 150001 Harbin, People's Republic of China; and [f]Department of Physics and Texas Center for Superconductivity, University of Houston, Houston, TX 77204

Zintl compounds are considered to be potential thermoelectric materials due to their "phonon glass electron crystal" (PGEC) structure. A promising Zintl-phase thermoelectric material, 2-1-2–type Eu₂ZnSb₂ ($P6_3/mmc$), was prepared and investigated. The extremely low lattice thermal conductivity is attributed to the external Eu atomic layers inserted in the $[Zn_2Sb_2]^{2-}$ network in the structure of 1-2-2–type EuZn₂Sb₂ ($P\bar{3}m1$), as well as the abundant inversion domain boundary. By regulating the Zn deficiency, the electrical properties are significantly enhanced, and the maximum ZT value reaches ~1.0 at 823 K for Eu₂Zn₀.₉₈Sb₂. Our discovery provides a class of Zintl thermoelectric materials applicable in the medium-temperature range.

thermoelectric properties | Zintl phase | low thermal conductivity | Eu₂ZnSb₂

Thermoelectric (TE) materials have attracted considerable interest during the past few decades due to their promising capability of converting waste heat into electricity (1–3). The TE conversion efficiency is governed by the dimensionless figure-of-merit $ZT = \sigma S^2 T/\kappa$, where S is the Seebeck coefficient, σ is the electrical conductivity, κ is the total thermal conductivity [κ is the sum of the lattice thermal conductivity (κ_L), the charge-carrier thermal conductivity (κ_c), and the bipolar thermal conductivity (κ_B)], and T is the absolute temperature (4, 5). The strong coupling between S, σ, and κ_c makes increasing ZT difficult. A straightforward way is to decrease the lattice thermal conductivity, which is the only independent material property. Nanoengineering and point-defect engineering have been demonstrated to be effective in enhancing the phonon scattering and decreasing the lattice thermal conductivity (6, 7). In addition, searching for compounds with intrinsic complex structure and low lattice thermal conductivity has also been proved feasible for achieving high-performance TE materials, such as SnSe (8–10), BiCuSeO (11, 12), clathrates (13), skutterudites (7, 14, 15), Ag₉GaSe₆ (16), Cu₂Se (17), AgSbTe₂ (18), Zintl compounds (19), etc.

The Zintl phase is a prototype of the phonon glass electron crystal (PGEC) concept. Zintl anions provide the diverse electronic structure as the "electron crystal" and Zintl cations play the role of the "phonon scattering center" for an extremely low lattice thermal conductivity. To date, Zintl phases with excellent TE properties mainly include AB_2X_2 (1-2-2–type) (20–22), $A_{14}BX_{11}$ (14-1-11–type) (23–25), $A_9B_{4.5}X_9$ (9-4.5-9–type) (26–28), and $A_5B_2X_6$ (5-2-6–type) (29, 30), among others (A is an alkaline-earth or divalent rare-earth element, B is a main-group element or transition metal, and X is Sb or Bi). Among them, AB_2X_2–type Zintl compounds (EuZn₂Sb₂, CaZn₂Sb₂, YbZn₂Sb₂, YbCd₂Sb₂, etc.) have been the most widely investigated. A ZT ~0.8 at 723 K was obtained in EuZn₂Sb₂ with room-temperature lattice thermal conductivity of ~2.6 W m⁻¹·K⁻¹ (31). Even lower lattice thermal conductivity and higher ZT values have been achieved by isoelectronic alloying with Ca or Yb at the A site and Cd or Mn at the B site (31, 32). For example, the room-temperature lattice thermal conductivity decreases from ~2.6 to

~1.5 W m⁻¹·K⁻¹, and the higher-temperature (773 K) lattice thermal conductivity decreases from ~1.1 to ~0.7 W m⁻¹·K⁻¹ when alloying 50 at % CaZn₂Sb₂ in EuZn₂Sb₂ (31).

Here we found that an intrinsically ultralow lattice thermal conductivity (~0.4 W m⁻¹·K⁻¹ from 300 to 623 K) could be obtained by inserting external Eu atoms into the $[Zn_2Sb_2]^{2-}$ network in the structure of 1-2-2–type EuZn₂Sb₂ ($P\bar{3}m1$), which then changed to Eu₂ZnSb₂ [2-1-2–type structure ($P6_3/mmc$)]. Compared with the structure of EuZn₂Sb₂, Eu₂ZnSb₂ contains external Eu atomic layers as the phonon scattering center, which is similar to the Rh honeycomb layers inserted in the PrRh₃B₂ blocks, leading to anomalous low total thermal conductivity (33). Furthermore, Zn vacancies could be introduced to increase the electrical conductivity and suppress the bipolar effect. Benefiting from the enhanced power factor and its intrinsic low lattice thermal conductivity, a ZT value of ~1.0 was achieved in Eu₂Zn₀.₉₈Sb₂ at 823 K. The discovery of the 2-1-2–type Zintl TE materials may provide a system with which to explore higher ZT.

Results and Discussion

The crystal structure of Eu₂ZnSb₂ (2-1-2–type) can be viewed as external Eu atomic layers inserted into the $[Zn_2Sb_2]^{2-}$ network of EuZn₂Sb₂ (1-2-2–type) (Fig. 1A). After that, the position of Zn

Significance

Searching for compounds with intrinsic low lattice thermal conductivity has been proven a successful strategy for achieving high thermoelectric performance. Here we report a promising 2-1-2–type Eu₂ZnSb₂ ($P6_3/mmc$) Zintl-phase thermoelectric material. Its intrinsic crystal structure, together with its widely distributed plane defects, likely contribute to its effective phonon scattering, leading to ultralow thermal conductivity (~0.41 W m⁻¹·K⁻¹ at 300 K and ~0.37 W m⁻¹·K⁻¹ at 623 K), lower than that of most other Zintl compounds. By regulating the Zn deficiency, the maximum ZT value of Eu₂Zn₀.₉₈Sb₂ reaches ~1.0 at 823 K, which is quite respectable for p-type Zintl materials. This discovery provides a class of Zintl thermoelectric materials applicable in the medium-temperature range.
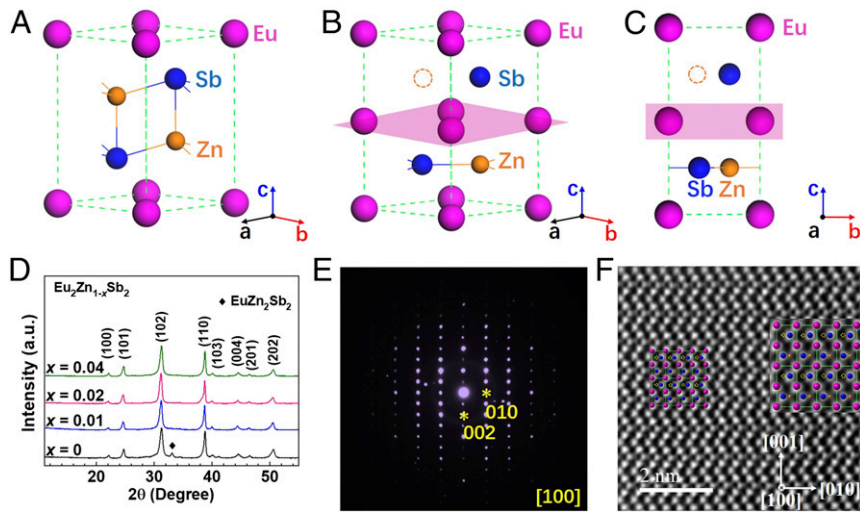
Fig. 1. Structure characterizations of the Eu_2ZnSb_2 Zintl phase. Structural comparison of (*A*) $EuZn_2Sb_2$ and (*B*) Eu_2ZnSb_2. The purple, blue, and orange spheres represent the europium, antimony, and zinc, respectively. (*C*) Structure projection along the [100] direction of Eu_2ZnSb_2. (*D*) XRD patterns of $Eu_2Zn_{1-x}Sb_2$ (*x* = 0, 0.01, 0.02, and 0.04). (*E*) SAED pattern taken along the [100] direction. (*F*) HADDF-STEM image along the [100] direction of $Eu_2Zn_{0.98}Sb_2$ matched with the projection structure of Eu_2ZnSb_2.

changed slightly along the *c* axis (Fig. 1 *B* and *C*). It is clear that this $[Eu^{2+}]_2$ $[Zn^{2+}]_2$ $[Sb^{3-}]_2$ system is charge-imbalanced, requiring a 50% occupancy at the Zn site to balance the electronic state (34). This structure of Eu_2ZnSb_2 ($P6_3/mmc$) is similar to that of the previously reported LiZnSb– and CaAgSb–type Zintl compounds ($P6_3mc$) (35, 36). However, one additional plane of symmetry exists in this Eu_2ZnSb_2 structure. Fig. 1*D* shows the X-ray diffraction (XRD) patterns of $Eu_2Zn_{1-x}Sb_2$ (*x* = 0, 0.01, 0.02, and 0.04) prepared directly by ball milling and hot pressing. A trace of a secondary phase (mainly $EuZn_2Sb_2$) can be found in the Eu_2ZnSb_2 sample. Single-phase $Eu_2Zn_{1-x}Sb_2$ with a hexagonal structure was obtained by reducing the Zn content. The selected area electron diffraction (SAED) pattern taken along the [100] direction (shown in Fig. 1*E*) is consistent with the hexagonal structure of the $P6_3/mmc$ space group. Fig. 1*F* shows the C_s-corrected high-angle annular dark-field scanning transmission electron microscopy (HAADF-STEM) image of $Eu_2Zn_{0.98}Sb_2$. It is well known that HAADF-STEM offers a unique technique to image the crystal structure correctly. Unlike that of conventional TEM images, the contrast of HAADF-STEM images is roughly proportional to $Z^{1.7}$, where Z is the atomic number. Thus, the brightest atomic column in Fig. 1*F* is Eu (Z = 63) and the next brightest is Sb (Z = 51), while Zn atoms, with a smaller atomic number (Zn = 30), appear darker in the image. The atomic sites match well with the [100] structure projection

(shown in Fig. 1*C*). We can clearly see that half sites (yellow circles) are not occupied by Zn atoms, which indicates a 50% occupancy of Zn in this crystal.

A state-of-the-art ZT ~1.0 at 823 K was achieved in $Eu_2Zn_{0.98}Sb_2$, which is higher than that of $EuZn_2Sb_2$ (dotted lines in Fig. 2*A*) (20, 37). This high ZT is attributed to the intrinsic low lattice thermal conductivity and the increased electrical conductivity due to the Zn vacancy. As shown in Fig. 2*B*, in the temperature range from 300 to 823 K, $Eu_2Zn_{0.98}Sb_2$ outperforms the current popular optimized p-type Zintl TE materials, including the 3-1-3 ($Ca_{2.97}Na_{0.03}AlSb_3$) –, 11-6-12 ($Eu_{11}Cd_{4.5}Zn_{1.5}Sb_{12}$)–, 1-2-2 ($Ca_{0.25}Yb_{0.75}Zn_2Sb_2$) –, and 5-2-6 ($Ca_{4.75}Na_{0.25}Al_2Sb_6$)–types, among others (24, 31, 37–40), suggesting that it is a promising medium-temperature TE material.

The temperature-dependent electrical conductivity, Seebeck coefficient, and power factor of $Eu_2Zn_{1-x}Sb_2$ (*x* = 0, 0.01, 0.02, and 0.04) are shown in Fig. 3. The electrical conductivity of all of the samples decreases with increasing temperature, showing a degenerate semiconductor behavior at lower temperature, and increases at higher temperature because of the thermally activated carriers (Fig. 3*A*). With increasing Zn deficiency, it is clear that the electrical conductivity increases due to the increased Hall carrier concentration (Fig. 4 *A* and *B*) and Hall mobility (Fig. 4*C*). As shown in Fig. 3*B*, the Seebeck coefficient decreases, and the peak value of each composition is gradually shifted to
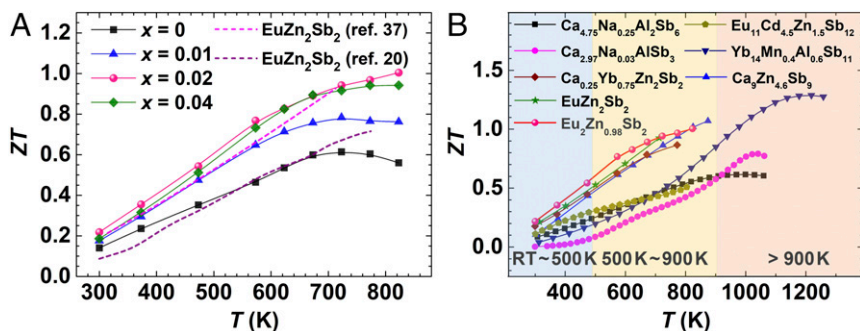

Fig. 2. Comparison of ZT values. (*A*) Temperature-dependent ZT values of $Eu_2Zn_{1-x}Sb_2$ (*x* = 0, 0.01, 0.02, and 0.04). ZT values of $EuZn_2Sb_2$ prepared by different groups are included for comparison (20, 37). (*B*) Temperature-dependent ZT values of some state-of-the-art p-type Zintl-phase TE materials (24, 31, 37–40).
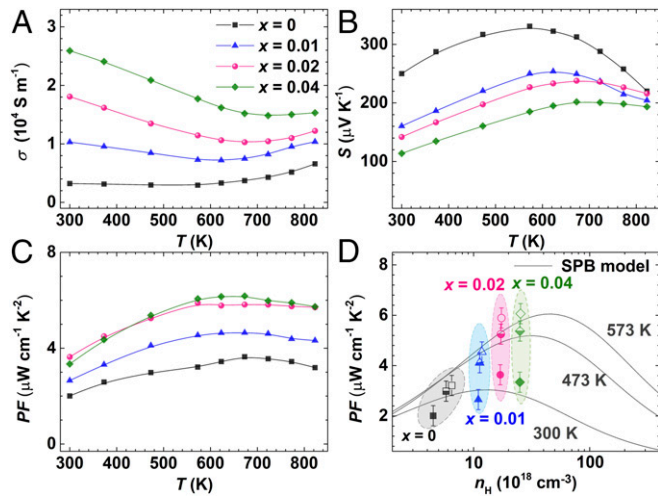
Fig. 3. Temperature-dependent electrical transport properties for $Eu_2Zn_{1-x}Sb_2$ (x = 0, 0.01, 0.02, and 0.04). (*A*) Electrical conductivity, (*B*) Seebeck coefficient, and (*C*) *PF*. (*D*) Hall carrier concentration-dependent *PF* of $Eu_2Zn_{1-x}Sb_2$ (x = 0, 0.01, 0.02, and 0.04) at different temperatures [i.e., 300 K (filled symbols), 473 K (half-filled symbols), and 573 K (open symbols)]. The solid lines are calculated by the SPB model with the effective mass ~0.5 m_0.

higher temperature as x increases. This small fraction of Zn vacancy dramatically improves the electrical properties, leading to a 100% enhancement in power factor ($PF = S^2\sigma$) (Fig. 3*C*). The maximum power factor is ~6.2 μW cm^{-1}·K^{-2} at 673 K for $Eu_2Zn_{0.96}Sb_2$, comparable to the optimal $Ca_9Zn_{4.5}Sb_9$ (~6.6 μW cm^{-1}·K^{-2} at 710 K) (41) and $Ca_5Al_2Sb_6$ (~5.4 μW cm^{-1}·K^{-2} at 750 K) (40). Fig. 3*D* presents the relationship between the *PF* and the Hall carrier concentration at different temperatures, together with the theoretical prediction by the single parabolic band (SPB) model (effective mass m^* = 0.5 m_0, as shown in *SI Appendix*, Fig. S1). A more accurate prediction would be expected from using the two-band Kane model (or the multiband model) with a detailed band structure. The increased carrier concentration contributes to the notable *PF*, which is close to the maximum values at different temperatures.

To further clarify the transport mechanism, we measured the Hall coefficient from room temperature to 773 K, as shown in Fig. 4*A*. A bipolar effect clearly occurs in Eu_2ZnSb_2 at temperatures higher than 500 K. The bipolar effect of Eu_2ZnSb_2 might be related to the low-room-temperature Hall carrier concentration (~4.5 × 10^{18} cm^{-3}) and the narrow band gap (~0.17 eV, plotted in Fig. 4*D*), which are lower and narrower than those of $EuZn_2Sb_2$ (~3.5 × 10^{19} cm^{-3} and ~0.5 eV), respectively (20). After the introduction of Zn vacancies, the Hall carrier concentration of $Eu_2Zn_{1-x}Sb_2$ increases from ~4.5 × 10^{18} cm^{-3} to ~2.5 × 10^{19} cm^{-3} at 300 K, close to the vacancy doping limit (Fig. 4*B*), and the estimated optical band gap increases to larger than 0.2 eV. As a result, both the increased band gap and Hall carrier concentration postpone the bipolar effect to higher temperatures. The room-temperature Hall mobility (μ_H) of Eu_2ZnSb_2 is ~49 cm^2 V^{-1}·s^{-1}, which is lower than those of other samples (~60–70 cm^2 V^{-1}·s^{-1}) due to the obvious secondary phase for the electron scattering existing in this undoped sample. The Zn deficiency can help to avoid this impurity, leading to a higher Hall mobility. The μ_H appears to have a $\mu_H \propto T^{-1.5}$ relationship (shown in Fig. 4*C*), indicating that acoustic phonon scattering dominates at high temperature for all of the samples.

The temperature-dependent total thermal conductivity (κ) was calculated and is plotted in Fig. 5*A*. We used the measured specific heat for the calculation, which is higher than the estimated value by Dulong Petit law (Fig. 5*A*, *Inset*). The room-

temperature total thermal conductivity of Eu_2ZnSb_2 is as low as ~0.4 W m^{-1}·K^{-1}, which is lower than most of the high-performance TE materials (42, 43). With increasing Zn deficiency, the total thermal conductivity increases due to the carrier contribution, but remains lower than 0.6 W m^{-1}·K^{-1} over the whole measured temperature range. The carrier contribution (κ_c) can be estimated by $\kappa_c = L\sigma T$, where L is the Lorenz number. Here, we used the SPB model under the assumption of acoustic phonon scattering to estimate the Lorenz number as for other reported Zintl TE materials (as shown in *SI Appendix*, Fig. S2). We subtracted κ_c from κ and display the lattice thermal conductivity in Fig. 5*B*. The dashed line indicates the estimated amorphous limit for the lattice thermal conductivity (κ_{glass}) calculated from Cahill's method assuming that the phonon mean-free path is a half of the phonon wavelength according to the following expression (41):

$$\kappa_{glass} = \frac{1}{2}\left(\frac{\pi}{6}\right)^{1/3} k_B V^{(-2/3)}(2v_T + v_L),$$ **[1]**

where k_B is the Boltzmann constant and V is the average volume per atom. Room-temperature transverse (v_T) and longitudinal (v_L) components of the sound velocity are ~1,900 and ~3,170 m s^{-1}, respectively. As shown in Fig. 5*B*, the lattice thermal conductivity displays a near-$\kappa_L \propto T^{-1}$ relationship at lower temperature, indicating the existence of Umklapp scattering (44). When the temperature is higher than 650 K, the lattice thermal conductivity increases slightly due to the onset of bipolar conduction. With increasing Zn deficiency, κ_L is reduced due to the increased point-defect scattering, and the bipolar thermal conductivity is clearly depressed by the higher number of majority carriers. It should be noted that extremely low lattice thermal conductivities (lower than κ_{glass}) have also been previously observed in some other Zintl compounds (28, 41, 44, 45). This problem might be related to the calculation of the Lorenz number. Complex band structures make the SPB model inaccurate, and the relationship between L and the Seebeck coefficient becomes more complicated (41, 46).

In Fig. 5*C*, we compared the κ_L of $Eu_2Zn_{0.98}Sb_2$ with that of the well-known 1-2-2–type Zintl compounds. $CaZn_2Sb_2$, $EuZn_2Sb_2$, and $EuMg_2Bi_2$ possess relatively high lattice thermal conductivities (red region) (31, 47). With binary and even ternary alloying, the
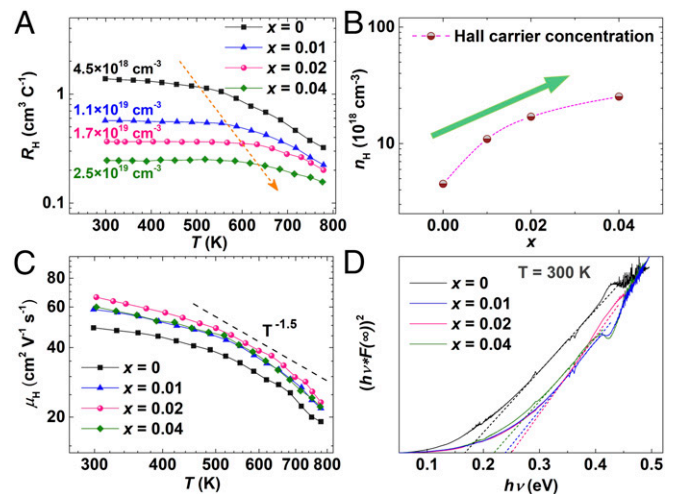

Fig. 4. Temperature-dependent Hall measurements and room-temperature band-gap measurements. (*A*) Temperature-dependent Hall coefficient, (*B*) relationship between the room-temperature Hall carrier concentration and the composition, (*C*) temperature-dependent Hall mobility, and (*D*) normalized optical absorption versus photon energy for $Eu_2Zn_{1-x}Sb_2$ (x = 0, 0.01, 0.02, and 0.04).

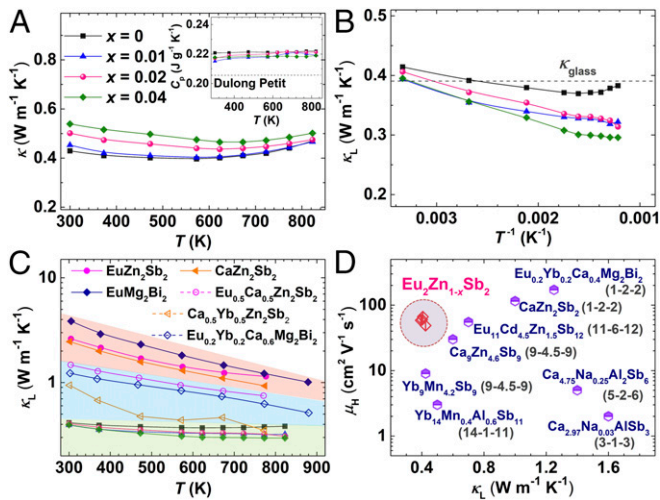**Fig. 5.** Temperature-dependent thermal transport properties for Eu$_2$Zn$_{1-x}$Sb$_2$ (x = 0, 0.01, 0.02, and 0.04). (*A*) Total thermal conductivity and (*B*) lattice thermal conductivity. Specific heat as a function of temperature is shown in *A* (*Inset*). The calculated minimum lattice thermal conductivity is plotted in *B* (dashed line). (*C*) Lattice thermal conductivity as a function of temperature for Eu$_2$Zn$_{1-x}$Sb$_2$ (x = 0, 0.01, 0.02, and 0.04). Temperature-dependent lattice thermal conductivity values of 1–2–2–type Zintl compounds are included for comparison. (*D*) Room-temperature Hall mobility versus lattice thermal conductivity of representative Zintl phases (24, 31, 38–41, 44, 47).

lattice thermal conductivity is reduced significantly to near or lower than 1.0 W m^{-1}·K^{-1} (blue region). Clearly, the lattice thermal conductivity of Eu$_2$Zn$_{1-x}$Sb$_2$ is much lower, which possibly be attributed to more cations like Eu atomic layers inserted into the [Zn$_2$Sb$_2$]$^{2-}$ network serving as phonon-scattering centers and to the complex microstructure (discussed below). Moreover, defect sites of Zn make the crystal structure more asymmetric than 1-2-2–type Zintl compounds, and effectively cause phonon scattering (46). To exclude the effect of nanostructure, we also prepared another

Eu$_2$ZnSb$_2$ sample by melting, hand milling, and hot pressing. The lattice thermal conductivity of this sample is presented in *SI Appendix,* *Fig. S3E*, which is also much lower than that of EuZn$_2$Sb$_2$, confirming the effect of the intrinsic crystal structure of Eu$_2$ZnSb$_2$. The further decreased lattice thermal conductivity in the ball-milled sample is due to the nanostructure. In Fig. 5*D*, the Hall mobility versus lattice thermal conductivity of different p-type Zintl materials is displayed (24, 31, 38–41, 44, 47). Normally, a dimensionless material parameter B has proven to be useful in evaluating a material's TE performance (48):

$$B = 5.745 \times 10^{-6} \frac{\mu(m^*/m_0)^{3/2}}{\kappa_L} T^{5/2},\qquad [2]$$

where m^*, m_0, μ, κ_L, and T are the carrier effective mass, electron mass, carrier mobility, lattice thermal conductivity, and absolute temperature, respectively. It is noteworthy that high carrier mobility (μ) and low lattice thermal conductivity (κ_L) will lead to a large B value. The Eu$_2$ZnSb$_2$ compounds exhibit κ_L as low as that of Yb$_9$Mn$_{4.2}$Sb$_9$ (44) but μ as high as that of Eu$_{11}$Cd$_{4.5}$Zn$_{1.5}$Sb$_{12}$ (38). These properties point to the promising TE performance of Eu$_2$ZnSb$_2$.

To clearly reveal the atomic-scale microstructural features of the nanostructured Eu$_2$Zn$_{0.98}$Sb$_2$, TEM and HAADF-STEM investigations were carried out. Fig. 6 *A* and *B* is low-magnification TEM images of the Eu$_2$Zn$_{0.98}$Sb$_2$ sample, which display the clear grain boundaries with grain sizes between 200 and 500 nm. This small size should contribute to the effective phonon scattering for the lower lattice thermal conductivity. Some string contrasts can be observed as indicated by arrows in Fig. 6 *A* and *B*, and are ubiquitous throughout the Eu$_2$Zn$_{0.98}$Sb$_2$ sample. The cause of the string contrasts will be analyzed at the atomic level in the following discussion. The adjacent crystal grains possessing [100] and [310] orientation with the sharp grain boundary (GB) marked by the dashed line in Fig. 6*C* show the highly crystallized nature of nanostructured Eu$_2$Zn$_{0.98}$Sb$_2$. A high-magnification [100] HAADF-STEM image is shown in Fig. 6*D*. The widely distributed planar defect of the inversion domain boundary (IDB) is considered to be the main
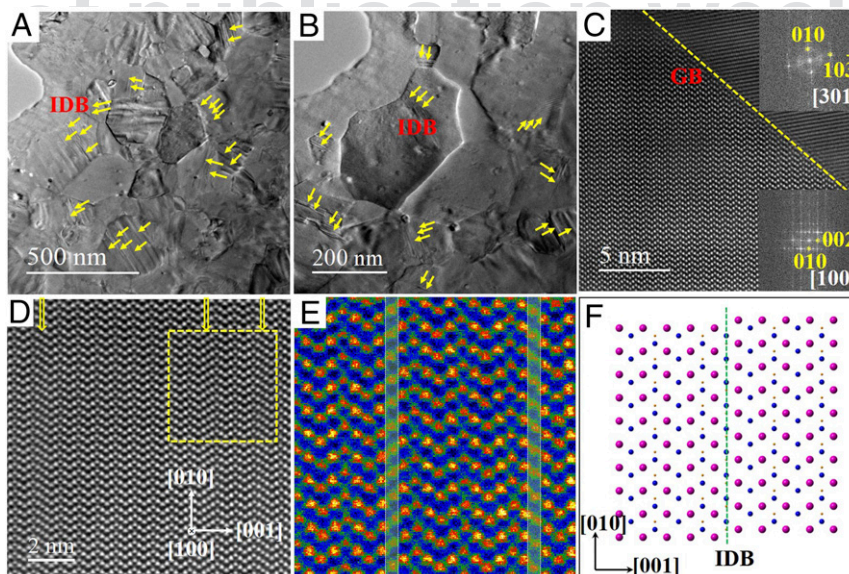

Fig. 6. Typical microstructures for Eu$_2$Zn$_{0.98}$Sb$_2$. (*A* and *B*) Low-magnification TEM images of Eu$_2$Zn$_{0.98}$Sb$_2$. The string contrasts indicated by arrows are caused by the IDB. (*C*) HADDF-STEM image of the adjacent crystal grains with [100] and [301] orientation, with the sharp GB marked by the dashed line. (*D*) [100] HADDF-STEM image for IDB with the extra atomic layers indicated by arrows. (*E*) Magnified view of the yellow boxed region in *D*. (*F*) Atomic configuration of the IDB along the [100] direction. Two domains are related by inversion at the Sb position. The purple, blue, and orange spheres represent the europium, antimony, and zinc, respectively.

factor that reduces lattice thermal conductivity in the $Eu_2Zn_{0.98}Sb_2$ sample. The extra atomic layers marked by the arrows indicate that the planar defects exist in the $Eu_2Zn_{0.98}Sb_2$ crystal, and correspond to the string contrasts in the low-magnification TEM images in Fig. 6 *A* and *B*. The rectangular region in Fig. 6*D* is enlarged in Fig. 6*E*, where the extra atomic layer (yellow region) can be clearly seen. Based on Fig. 6*E*, the proposed atomic configuration of the IDB along the [100] direction is shown in Fig. 6*F*. The two domains are related by inversion at the Sb position at the boundary.

Conclusion

In summary, we investigated the structure and thermoelectric properties of the Eu_2ZnSb_2 Zintl phase. The intrinsic crystal structure and the widely distributed plane defects contribute to its ultralow thermal conductivity. The Zn deficiency clearly improves the electrical properties by introducing holes to the compounds. As a result, a ZT value ~1.0 at 823 K is achieved for $Eu_2Zn_{0.98}Sb_2$. This study provides us a promising thermoelectric material for medium-temperature applications. Further optimization by doping or alloying is expected to lead to even higher thermoelectric performance.

Experimental Methods

Sample Preparation. Europium (Eu, 99.9%, chunk), zinc (Zn, 99.999%, powder), and antimony (Sb, 99.999%, shot) were weighed according to the stoichiometry of $Eu_2Zn_{1-x}Sb_2$ ($x = 0$, 0.01, 0.02, and 0.04). The raw materials were loaded into a stainless-steel jar with stainless-steel balls in an argon-filled glove box, and then ball milled by a high-energy ball mill (SPEX 8000M) for 10 h. The obtained powder was loaded into a graphite die with an inner diameter of 12.7 mm and consolidated at 853 K for 2 min by a direct-current–induced hot pressing under an axial pressure of 50 MPa.

Sample Characterization. The crystal structures were examined by XRD (Rigaku D/max 2500 PC). The microstructures were investigated by a spherical aberration-corrected (C_s-corrected) electron microscope (JEM-ARM200F). The Seebeck coefficient (S) and electrical conductivity (σ) were simultaneously measured using a commercial apparatus (ZEM-3, Advance-Riko). The thermal conductivity (κ) was calculated by $\kappa = D\alpha C_p$, where D is the volumetric density determined by the Archimedes method, α is the thermal diffusivity measured using a laser flash apparatus (Netzsch LFA 457), and C_p is the specific heat obtained using a differential scanning calorimetry thermal analyzer (Netzsch DSC 404 F3). The temperature-dependent Hall coefficients (R_H) were measured using the van der Pauw technique under a reversible magnetic field of 1.5 T. The Hall carrier concentration n_H and Hall mobility μ_H were calculated using $n_H = 1/(eR_H)$ and $\mu_H = \sigma R_H$, respectively. Room-temperature optical diffuse reflectance spectra of the powders were detected using a FTIR system (Thermo Fisher Nicolet iS50). The longitudinal (v_L) and transverse (v_T) components of the sound velocity were measured using an ultrasonic pulse receiver (Olympus) equipped with an oscilloscope (Tektronix). The uncertainty for the electrical conductivity is 3%, the Seebeck coefficient, 5%, and the thermal conductivity, 7% (comprising uncertainties of 4% for the thermal diffusivity and 3% for the density). As a result, the combined uncertainty for the PF is 10% and that for ZT value is 12%.

1. Li S, Li X, Ren Z, Zhang Q (2018) Recent progress towards high performance of tin chalcogenide thermoelectric materials. *J Mater Chem A* 6:2432–2448.
2. Liu W, et al. (2017) New trends, strategies and opportunities in thermoelectric materials: A perspective. *Mater Today Phys* 1:50–60.
3. Zhao L, Kanatzidis MG (2016) An overview of advanced thermoelectric materials. *J Materiomics* 2:101–103.
4. Wu Y, et al. (2017) Promising thermoelectric performance in van der Waals layered SnSe₂. *Mater Today Phys* 3:127–136.
5. Zhu T, et al. (2017) Compromise and synergy in high-efficiency thermoelectric materials. *Adv Mater* 29:1605884.
6. Liu X, et al. (2016) Significant roles of intrinsic point defects in Mg2X(X= Si, Ge, Sn) thermoelectric materials. *Adv Electron Mater* 2:1500284.
7. Mori T (2017) Novel principles and nanostructuring methods for enhanced thermoelectrics. *Small* 13:1702013.
8. Li S, et al. (2018) Heavy doping by bromine to improve the thermoelectric properties of n-type polycrystalline SnSe. *Adv Sci (Weinh)* 5:1800598.
9. Chang C, et al. (2018) 3D charge and 2D phonon transports leading to high out-of-plane ZT in n-type SnSe crystals. *Science* 360:778–783.
10. Zhao LD, et al. (2016) Ultrahigh power factor and thermoelectric performance in hole-doped single-crystal SnSe. *Science* 351:141–144.
11. Liu Y, et al. (2016) Synergistically optimizing electrical and thermal transport properties of BiCuSeO via a dual-doping approach. *Adv Energy Mater* 6:1502423.
12. Sui J, et al. (2013) Texturation boosts the thermoelectric performance of BiCuSeO oxyselenides. *Energy Environ Sci* 6:2916–2920.
13. Chen C, Zhang L, Dong J, Xu B (2016) Thermoelectric performance of Yb-doped Ba₈Ni₀.₁Zn₀.₅₄Ga₁₃.₈Ge₃₁.₅₆ type-I clathrate synthesized by high-pressure technique. *J Electron Mater* 46:2860–2866.
14. Shi X, et al. (2011) Multiple-filled skutterudites: High thermoelectric figure of merit through separately optimizing electrical and thermal transports. *J Am Chem Soc* 133:7837–7846.
15. Slack GA, Tsoukala VG (1994) Some properties of semiconducting IrSb₃. *J Appl Phys* 76:1665–1671.
16. Jiang B, et al. (2018) Entropy optimized phase transitions and improved thermoelectric performance in n-type liquid-like Ag₉GaSe₆ materials. *Mater Today Phys* 5:20–28.
17. Zhao K, et al. (2017) Ultrahigh thermoelectric performance in Cu₂₋ySe₀.₅S₀.₅ liquid-like materials. *Mater Today Phys* 1:14–23.
18. Hong M, et al. (2018) Achieving zT > 2 in p-type AgSbTe₂₋ₓSeₓ alloys via exploring the extra light valence band and introducing dense stacking faults. *Adv Energy Mater* 8:1702333.
19. Shuai J, et al. (2017) Recent progress and future challenges on thermoelectric Zintl materials. *Mater Today Phys* 1:74–95.
20. Wang X, et al. (2017) Single parabolic band transport in p-type EuZn₂Sb₂ thermoelectrics. *J Mater Chem A* 5:24185–24192.
21. Mao J, et al. (2017) Anomalous electrical conductivity of n-type Te-doped Mg₃.₂Sb₁.₅Bi₀.₅. *Mater Today Phys* 3:1–6.
22. Chen C, et al. (2018) Enhanced thermoelectric performance of p-type Mg₃Sb₂ by lithium doping and its tunability in an anionic framework. *J Mater Sci* 53:16001–16009.
23. Yu C, et al. (2012) Improved thermoelectric properties in Lu-doped Yb₁₄MnSb₁₁ Zintl compounds. *Appl Phys Express* 5:031801.
24. Toberer ES, et al. (2008) Traversing the metal-insulator transition in a Zintl phase: Rational enhancement of thermoelectric efficiency in Yb₁₄Mn₁₋ₓAlₓSb₁₁. *Adv Funct Mater* 18:2795–2800.
25. Kastbjerg S, et al. (2011) Multi-temperature synchrotron powder X-ray diffraction study and Hirshfeld surface analysis of chemical bonding in the thermoelectric Zintl phase Yb₁₄MnSb₁₁. *Chem Mater* 23:3723–3730.
26. Xia SQ, Bobev S (2007) Interplay between size and electronic effects in determining the homogeneity range of the A9Zn4+xPn9 and A9Cd4+xPn9 phases (0 < or = x < or = 0.5), A = Ca, Sr, Yb, Eu; Pn = Sb, Bi. *J Am Chem Soc* 129:10011–10018.
27. Ohno S, Zevalkink A, Takagiwa Y, Bux SK, Snyder GJ (2014) Thermoelectric properties of the Yb₉Mn₄.₂₋ₓZnₓSb₉ solid solutions. *J Mater Chem A* 2:7478–7483.
28. Wu Z, et al. (2016) Tuning the thermoelectric properties of Ca₉Zn₄₊ₓSb₉ by controlled doping on the interstitial structure. *Chem Mater* 28:6917–6924.
29. Aydemir U, et al. (2015) Thermoelectric properties of the Zintl phases Yb₅M₂Sb₆ (M = Al, Ga, In). *Dalton Trans* 44:6767–6774.
30. Zevalkink A, et al. (2012) Influence of the triel elements (M= Al, Ga, In) on the transport properties of Ca₅M₂Sb₆ Zintl compounds. *Chem Mater* 24:2091–2098.
31. Shuai J, et al. (2016) Enhancement of thermoelectric performance of phase pure Zintl compounds Ca₁₋ₓYbₓZn₂Sb₂, Ca₁₋ₓEuₓZn₂Sb₂, and Eu₁₋ₓYbₓZn₂Sb₂ by mechanical alloying and hot pressing. *Nano Energy* 25:136–144.
32. Zhang H, et al. (2010) Thermoelectric properties of Eu(Zn₍₁₋ₓ₎Cd₍ₓ₎)₂Sb₂. *Dalton Trans* 39:1101–1104.
33. Kakefuda Y, et al. (2017) Thermal conductivity of PrRh₄.₈B₂, a layered boride compound. *APL Mater* 5:126103.
34. Wilson DK, Saparov B, Bobev S (2011) Synthesis, crystal structures and properties of the Zintl phases Sr₂ZnP₂, Sr₂ZnAs₂, A₂ZnSb₂ and A₂ZnBi₂ (A = Sr and Eu). *Z Anorg Allg Chem* 637:2018–2025.
35. Toberer ES, May AF, Scanlon CJ, Snyder GJ (2009) Thermoelectric properties of p-type LiZnSb: Assessment of ab initio calculations. *J Appl Phys* 105:063701.
36. Wang J, Liu XC, Xia SQ, Tao XT (2013) Ca₍₁₋ₓ₎RE₍ₓ₎Ag₍₁₋y₎Sb (RE = La, Ce, Pr, Nd, Sm; 0 ≤ x ≤ 1; 0 ≤ y ≤ 1): Interesting structural transformation and enhanced high-temperature thermoelectric performance. *J Am Chem Soc* 135:11840–11848.
37. Zhang H, et al. (2008) A new type of thermoelectric material, EuZn₂Sb₂. *J Chem Phys* 129:164713.
38. Kazem N, et al. (2015) High temperature thermoelectric properties of the solid-solution Zintl phase Eu₁₁Cd₆₋ₓZnₓSb₁₂. *Chem Mater* 27:4413–4421.

39. Zevalkink A, Toberer ES, Zeier WG, Flage-Larsen E, Snyder GJ (2011) Ca_3AlSb_3: An inexpensive, non-toxic thermoelectric material for waste heat recovery. *Energy Environ Sci* 4:510–518.

40. Toberer ES, Zevalkink A, Crisosto N, Snyder GJ (2010) The Zintl compound $Ca_5Al_2Sb_6$ for low-cost thermoelectric power generation. *Adv Funct Mater* 20:4375–4380.

41. Ohno S, et al. (2017) Achieving zT > 1 in inexpensive Zintl phase $Ca_9Zn_{4+x}Sb_9$ by phase boundary mapping. *Adv Funct Mater* 27:1606361.

42. Zhu H, et al. (2018) Discovery of ZrCoBi based half Heuslers with high thermoelectric conversion efficiency. *Nat Commun* 9:2497.

43. Zhang J, et al. (2017) Discovery of high-performance low-cost n-type Mg_3Sb_2-based thermoelectric materials with multi-valley conduction bands. *Nat Commun* 8:13901.

44. Bux SK, et al. (2014) Glass-like lattice thermal conductivity and high thermoelectric efficiency in $Yb_9Mn_{4.2}Sb_9$. *J Mater Chem A* 2:215–220.

45. Kazem N, Zaikina JV, Ohno S, Snyder GJ, Kauzlarich SM (2015) Coinage-metal-stuffed $Eu_9Cd_4Sb_9$: Metallic compounds with anomalous low thermal conductivities. *Chem Mater* 27:7508–7519.

46. Zhu M, et al. (2018) Defect modulation on $CaZn_{1-x}Ag_{1-y}Sb$ (0 < x < 1; 0 < y <1) Zintl phases and enhanced thermoelectric properties with high ZT plateaus. *J Mater Chem A* 6:11773–11782.

47. Shuai J, et al. (2016) Higher thermoelectric performance of Zintl phases $(Eu_{0.5}Yb_{0.5})_{1-x}Ca_xMg_2Bi_2$ by band engineering and strain fluctuation. *Proc Natl Acad Sci USA* 113:E4125–E4132.

48. Liu W, et al. (2016) New insight into the material parameter B to understand the enhanced thermoelectric performance of $Mg_2Sn_{1-x-y}Ge_xSb_y$. *Energy Environ Sci* 9:530–539.